4-7-2004

Decadal Variability of Circulation in the Arctic Ocean Retrieved From Climatological Data by a Variational Method

Dmitri A. Nechaev
University of Southern Mississippi, dmitri.nechaev@usm.edu

Max Yaremchuk
International Pacific Research Center

Motoyoshi Ikeda
Hokudai University

Decadal variability of circulation in the Arctic Ocean retrieved from climatological data by a variational method

Dmitri Nechaev
Department of Marine Science, University of Southern Mississippi, Stennis Space Center, Mississippi, USA

Max Yaremchuk
International Pacific Research Center, Honolulu, Hawaii, USA

Motoyoshi Ikeda
Department of Earth and Environmental Sciences, Hokudai University, Sapporo, Japan

Received 9 December 2002; revised 2 December 2003; accepted 2 January 2004; published 7 April 2004.

[1] An inverse 3D finite-element ocean circulation model has been designed and used to study variability of the Arctic Ocean circulation in the last 4 decades. We obtained stationary model solutions with the temperature and salinity fields close to the ones given by the *Environmental Working Group* (*EWG*) [1998] atlas. Transports at the open boundaries, wind forcing and hydrographic fields are treated as unknowns, which are varied to minimize a quadratic cost function subject to model constraints. The inverse problem is solved for 10 gridded hydrographic data sets that were obtained as winter and summer averages of EWG data over each of the 4 decades (1950s to 1980s) and over the whole period of observations (1948–1993) documented in the atlas. The results show that Arctic circulation in the last 4 decades has undergone significant changes, which manifest themselves in (1) 10% reduction of the ventilation rate in the Atlantic sector of the Arctic Ocean; (2) substantial decrease of the advective heat and freshwater import at the lateral boundaries; (3) spinning down of the cyclonic gyre in the northern Greenland sea, which is partly driven by deep convection; and (4) 3400 km^3 increase of the net fresh water storage, with 75% taking place in the Atlantic sector of the Arctic Ocean. Most of these changes are similar to the ones observed on seasonal transition from winter to summer climatologies, and indicate that the Arctic Ocean is experiencing a shift toward a warmer state. *INDEX TERMS:* 4207 Oceanography: General: Arctic and Antarctic oceanography; 4215 Oceanography: General: Climate and interannual variability (3309); 4255 Oceanography: General: Numerical modeling; 4532 Oceanography: Physical: General circulation; *KEYWORDS:* finite elements, inverse modeling, Arctic Ocean, decadal variability

Citation: Nechaev, D., M. Yaremchuk, and M. Ikeda (2004), Decadal variability of circulation in the Arctic Ocean retrieved from climatological data by a variational method, *J. Geophys. Res.*, *109*, C04006, doi:10.1029/2002JC001740.

1. Introduction

[2] The Arctic Ocean (AO) is an important component of the climate system, but its role in global thermohaline circulation and climate change is not well understood. It is likely that long-term variations of the global climate are amplified in the Arctic by several feedback mechanisms including ice and snow melting that decreases surface albedo and atmospheric stability that traps seawater temperature anomalies near the surface. The Arctic, in turn, influences thermohaline circulation at lower latitudes by affecting deep convection in the North Atlantic through the freshwater (FW) export and by impact on global thermohaline forcing through atmospheric teleconnections like the Arctic and North Atlantic Oscillations [*Thompson and Wallace*, 1998; *Wallace*, 2000; *Wang and Ikeda*, 2000; *Ambaum et al.*, 2001].

[3] The important role of the Arctic in the climate system has fueled a large number of observational and modeling studies of AO. Perhaps the most resonant paper of recent years was published by *Rothrock et al.* [1999], who reported a tremendous (40%) decline of the AO ice thickness in the last 3 decades. Although the result was verified a year later by *Wadhams and Davis* [2000], *Holloway and Sou* [2002] provided model-based evidence that the ice volume has decreased much more slowly (10–15%) over the same period. Another important development in the study of AO long-term variability was put forward by *Proshutinsky and Johnson* [1997], who employed a wind-forced barotropic model and drifting buoy data to show that AO circulation undergoes consecutive changes between the cyclonic and anticyclonic regimes with a typical timescale of 7–10 years. *Rigor et*

0148-0227/04/2002JC001740

al. [2002] used drifting buoy data to provide observational evidence of a correlation between the surface currents and the Arctic Oscillation index. Recently, *Proshutinsky et al.* [2002b] pointed out the importance of the Beaufort Gyre and developed their concept of oscillatory behavior of the AO variability by including thermohaline interactions with the land/atmosphere.

[4] These and other recent developments in the studies of AO climate are hindered by a scarcity of long-term observational data and the complexity of numerical modeling. In the last 5 years, however, studies of the AO dynamics have been significantly intensified due to rapid increase of both the available data and computer capabilities. A large amount of in situ hydrographic data has been recently released through declassifying of the vast Russian archives [*EWG*, 1998; *Steele at al.*, 2001a]. Drifting buoy and satellite programs like IABP [*Rigor and Heiberg*, 1997] and SMMR-SSM/I [*Hollinger et al.*, 1987], on the other hand, provide a continuous stream of information on the ice cover and microwave spectrometry of the AO surface. State-of-the-art numerical models have been developed that are capable of simulating AO dynamics at 1/6° [*Zhang et al.*, 1999; *Zhang and Hunke*, 2001] to 1/12° resolutions (Polar Ice Prediction System, available at www.oc.nps.navy.mil/pips3). Together with process-oriented modeling efforts [*Proshutinsky and Johnson*, 1997; *Steele et al.*, 1996; *Karcher and Oberhuber*, 2002], these studies remain the major tool for investigating AO variability at large timescales.

[5] Regional AO models reproduce reasonably well the basic dynamics and thermodynamics of the Arctic, at least from the qualitative point of view. Quantitatively, there are striking differences among the models in capturing the mean or variability in heat and FW balances, sea level, sea ice, and 3D structures of the oceanic fields. For instance, AOMIP group [*Proshutinsky et al.*, 2001] revealed a persistent bias (as large as 1 ppt) in simulating the Beaufort Gyre salinity anomaly [see also *Steele et al.*, 2001b]. Uncertainties in the sea surface height (SSH) variability often reach 5–8 cm, which is comparable with the horizontal variation of the AO SSH field itself. These and other as yet unexplained problems with numerical modeling of the AO may be caused by a variety of reasons, which include errors in parameterization of subgrid processes and ice physics, uncertainties of the model forcing fields, and open boundary conditions. The latter play an especially important role in AO dynamics for two reasons. First, the AO is a relatively small basin, and the open boundary conditions (mass transports and property fluxes from the Atlantic and Pacific Oceans) have a large effect on internal circulation [e.g., *Karcher and Oberhuber*, 2002]. Second, ice cover prevents central AO from direct contact with atmosphere, and its ventilation is largely provided by lateral advection. Ice cover and sparsity of in situ observations are also the cause of large uncertainties in atmospheric forcing. River discharge as one of the most important thermohaline forcing factors [*Aagaard and Carmack*, 1989] is presently monitored with an accuracy of 30–50%. These and other forcing errors may accumulate during multi-year integrations of the numerical models and sometimes produce misleading results.

[6] A goal of the present study is to reconstruct the large-scale circulation in the AO and poorly known boundary conditions from the hydrographic data. We employ a 3D variational data assimilation scheme [*Nechaev et al.*, 2003] to combine the Environmental Working Group (EWG) seawater temperature and salinity data available in the internal regions of AO with the basic dynamical constraints, governing oceanic circulation at large timescales. The latter are the finite element (FE) discretizations of the steady-state momentum balance, hydrostatic, continuity, and the steady-state advection-diffusion equations for heat and salt. Assuming that EWG hydrology averaged over a decade provides a good estimate of the mean hydrographic fields, we search for the unknown transports at the open boundaries and the velocity field, which are capable of maintaining the observed 3D thermohaline structure within certain error bars prescribed by data statistics and by possible inaccuracy of the dynamical constraints.

[7] Though the data assimilation method retrieves the entire dynamically balanced 3D state, discussion in this paper is mainly focused on the characteristics that cannot be directly obtained by the dynamical method (transports through the open lateral boundaries, the total transport, and the large-scale sea surface height fields). Decadal variability of these quantities is assessed via inversion of the AO hydrological data sets averaged over 4 decades (starting from the 1950s) and over the whole period of observations documented in the EWG Atlas.

[8] In assessing the long-term AO variability, we rely heavily on data, whereas in diagnosing the 3D ocean state, numerical equations similar to those used in OGCMs are employed. In this respect, our study fills the gap between the purely statistical analyses of experimental data (which may include simple dynamics to diagnose the velocity field) and the numerical modeling studies that employ sophisticated dynamical constraints to assess oceanic variability. The benefits of such an approach are two-fold. First, we are able to estimate the barotropic component of the velocity directly from the data. This is important since diagnostic estimation of the AO currents via the thermal wind balance is more sensitive to the reference velocity field than in midlatitudes because of the weaker horizontal density gradients in polar seas. Besides, barotropic velocities account for 40–60% of the total kinetic energy and play an important role in AO dynamics. The second benefit is in obtaining an experimental estimate of the long-term variability of the open boundary transports. At decadal timescales they were never directly measured, but are considered to be one of the major driving mechanisms of the AO models owing to a relatively small size (and ventilation time) of the Arctic Basin [*Karcher and Oberhuber*, 2002]. In the present practice of AO numerical modeling, boundary transports are either prescribed from geostrophy and experimental estimates that may vary by 50–100% [*Proshutinsky et al.*, 2002a] or computed using ocean dynamics in a larger domain, often extending south as far as 40°N [*Zhang and Hunke*, 2001]. Results of our computations give independent estimates of these transports and may be useful in constraining high-resolution OGCMs since the former are consistent both with climatological *T*/*S* data and basic dynamics.

[9] The paper is organized as follows. Section 2 contains a brief description of the data and of the inverse model used for their processing. Section 3 describes seasonal variation of the AO state obtained through data assimilation of the seasonal climatologies. In section 4 we give an inventory of the total transport patterns computed by inverting the decadal data sets, discuss dynamics of the anomalies relative to the mean state diagnosed in the previous section, and analyze variability of the transports through the open lateral boundaries. Results of the study are summarized and discussed in section 5.

2. Data and Method

2.1. Data

[10] The primary data set analyzed in this study is the gridded hydrography of the Arctic Ocean. Salinity S and potential temperature θ are taken from the EWG (Environmental Working Group) digital atlas. Sixty-five percent of the data originate from the Russian classified archives, which were released under the Gore-Chernomyrdin environmental bilateral agreement. The data covers the depth range from 0 to 4 km at 22 levels, and are divided seasonally into winter (DJFMAM) and summer (JJASON) subsets. The gridded climatological fields were obtained by averaging over the 4 decades from the 1950s to the 1980s and over the whole period of documented observations (1948–1993). These data sets are hereinafter referred to as EWG50, EWG60, EWG70, EWG80, and EWGM for the mean climatology. EWG climatologies were derived from 354,000 stations distributed in the approximate proportion 2:3 between the winter and summer seasons. Coverage of the AO by stations is more or less homogeneous in time (e.g., 56, 56, 48, and 56 thousand stations for decadal summer climatologies), but strongly inhomogeneous in space, with only 5% of stations taken north of 80°N. Spectral optimal interpolation technique [*Kondratyev et al.*, 1995] was used to define the climatological fields on a homogeneous 50 × 50 km grid.

2.2. Model Constraints

[11] Our reconstruction of the large-scale circulation relies on the assumption that the unknown parameters (3D velocity $\mathbf{u}$, w, density ρ, pressure p) and the measured characteristics (potential temperature θ and salinity S) are not independent but are related to each other through the set of model constraints. We assume that outside Ekman boundary layers, the 3D large-scale velocity ($\mathbf{u}$, w) is well described by the geostrophic, hydrostatic, and continuity relationships,

$$\begin{aligned} f(\mathbf{k}\times\mathbf{u}) &= -\frac{1}{\rho_o}\nabla p + (\nabla\cdot K\nabla)\mathbf{u} + (K^v\mathbf{u}_z)_z, \\ 0 &= -p_z - \rho g, \\ \nabla\cdot\mathbf{u} + w_z &= 0, \\ \rho &= \mathcal{R}(\theta, S, p,). \end{aligned} \tag{1}$$

These expressions are considered as strong constraints in data assimilation procedure. Since open boundary transports and surface momentum fluxes are poorly known, the 2D barotropic component of the flow cannot be entirely reconstructed by equations (1) and hydrographic data. Therefore we additionally constrain the velocity field by the steady state heat and salt conservation relations written in the weak form,

$$\begin{aligned} \nabla(\mathbf{u}\theta) + (w\theta)_z &= (\nabla\cdot K_\theta\nabla)\theta + \left(K^v_\theta\theta_z\right)_z + \varepsilon_\theta \\ \nabla(\mathbf{u}S) + (wS)_z &= (\nabla\cdot K_S\nabla)S + \left(K^v_S S_z\right)_z + \varepsilon_S. \end{aligned} \tag{2}$$

The terms ε_θ and ε_S in equation (2) account for possible errors in the tracer advection-diffusion balances, associated with nonhydrostatic processes, parameterization errors, and long-term variability of the θ/S fields. Notation in equations (1) and (2) is conventional: p is pressure, ρ is density, ρ_o = 1025 kg/m^3, f is the Coriolis parameter, $\mathcal{R}$ stands for the nonlinear operator of the equation of seawater state proposed by *Ishizaki* [1994], and K, $K\theta$, and K_S denote diffusivity coefficients for momentum and tracers.

[12] No-slip boundary conditions and zero heat and salt fluxes are posed on the bottom. At the open boundaries $\partial\Omega$, we set Dirichlet boundary conditions for θ, S, and the normal velocity component v_n, and impose the free-slip condition on the velocity component tangent to the open boundary. To compute a solution of equations (1)–(2), we have to specify v_n on the open boundaries and on the surface momentum flux $\boldsymbol{\tau}(x, y)$ and ascribe certain values to the fields $\theta(x, y, z)$ and $S(x, y, z)$, which may deviate from the data within the observational error bars. The set of parameters $X = \{v_n(\partial\Omega), \boldsymbol{\tau}, \text{and } \theta, S\}$ constitute the control vector to be tuned in data assimilation algorithm. Given X, we solve equation (1) for $\mathbf{u}$, w, ρ, and p, and compute the residuals ε_θ and ε_S of the weak constraints (equation (2)) in the interior of the model domain.

[13] In the present study, we intentionally do not employ any ice model for computation of the surface momentum flux, and do not pose surface boundary conditions for equations (2) in the form of surface heat/FW fluxes. In contrast to the direct modeling, such an approach does not introduce any inconsistencies, because under the inverse formulation, model states are heavily constrained by observations.

[14] Since the available hydrographic data do not resolve boundary layers, we use a simplified parameterization of eddy diffusion. The momentum and tracer diffusion coefficients in the interior of the ocean are set to K = 500 m^2/s, $K_{\theta,S}$ = 300 m^2/s, and $K^v = K^v_{\theta,S}$ = 0.0002 m^2/s, respectively. Within the surface and bottom boundary layers, we used higher values for K^v corresponding to the Ekman layer thicknesses of 10 m and 25 m, respectively. To simulate lateral boundary layers, the magnitude of K and $K_{\theta,S}$ has been increased up to 4 times within the grid cells adjacent to the rigid boundaries.

[15] Equations (1) and (2) are discretized on the unstructured FE mesh (Figure 1) using the pseudo residual-free bubble function stabilization scheme [*Nechaev et al.*, 2003]. The mesh contains N = 24,437 nodes and N^e = 122,963 tetrahedral elements. The numbers of surface nodes and 2D triangular elements visible in Figure 1 are N_Γ = 1804 and $N_\Gamma{}^e$ = 3233. Bottom topography is taken from ETOP05 data set. The model grid spacing varies between 30 km in the

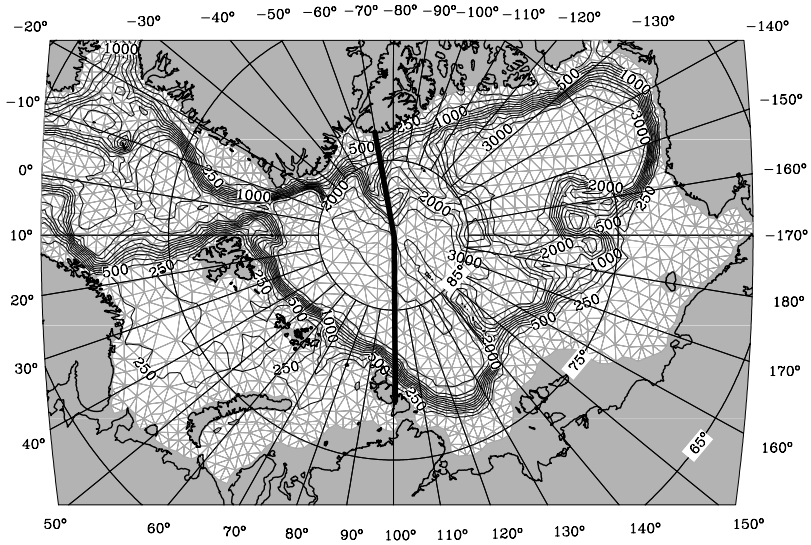

Figure 1. Bottom topography of the Arctic Ocean with the superimposed FE model mesh. Solid line denotes conventional boundary between the "Atlantic" and "Pacific" sectors of the Arctic Ocean.

regions with strong bottom topography gradients and 130 km in the open ocean. Most of the nodes of the FE mesh are vertically collocated with EWG data levels. Additional nodes and elements are introduced near the ocean floor for better approximation of bottom topography.

[16] Similar dynamical constraints were successfully implemented for 3D inversions of climatological data in the Antarctic marginal seas, and in the Atlantic sector of the Southern Ocean. Both finite-difference [*Grotov et al.*, 1998] and finite-element [*Nechaev et al.*, 2003] approaches have been used for discretization of equations (1)–(2).

2.3. Inversion Technique

[17] To retrieve the ocean state from the hydrographic data, a quadratic cost function,

$$\begin{aligned}\mathcal{J} = &\left\{\sum_{n=1}^{N} W_\theta(\mathbf{r},z)(\theta-\theta^*)^2+\sum_{n=1}^{N} W_S(\mathbf{r},z)(S-S^*)^2\right\}_{(\mathrm{I})}\\ &+\left\{\sum_{k=1}^{3} W_{V_k}\left(V_k-V_k^{\mathrm{fg}}\right)^2+\sum_{n=1}^{N_\Gamma} W_\tau(\mathbf{r})(\boldsymbol{\tau}-\boldsymbol{\tau}^{\mathrm{fg}})^2\right\}_{(\mathrm{II})}\\ &+\left\{\sum_{n=1}^{N^e}\left[W_\varepsilon^\theta(\mathbf{r},z)(\varepsilon_\theta)^2+ W_\varepsilon^S(\mathbf{r},z)(\varepsilon_S)^2\right]\right.\\ &\left.+\sum_{n=1}^{N_\Gamma^e}\left[\overline{W}_\varepsilon^\theta(\mathbf{r})(\bar{\varepsilon}_\theta)^2+ \overline{W}_\varepsilon^S(\mathbf{r})(\bar{\varepsilon}_S)^2\right]\right\}_{(\mathrm{III})}\\ &+\left\{\sum_{k=1}^{N^e} R_b(\mathbf{r},z)\parallel\mathbf{u}_b\parallel_k^2+\sum_{n=1}^{N} R_u(\mathbf{r},z)(\nabla\mathbf{u})^2\right\}_{(\mathrm{IV})},\end{aligned}\tag{3}$$

is minimized on the manifold that is defined by constraints (1) and (2) in the space of the AO state vectors $Y \equiv \{\mathbf{u}, w, \theta, S, \rho, p, \boldsymbol{\tau}\}$.

[18] Minimization starts from a first-guess model solution that is entirely defined by the first-guess control vector X^{fg}. The latter is built as follows. The θ^{fg} and S^{fg} fields are interpolated from the data; surface momentum fluxes $\boldsymbol{\tau}^{\mathrm{fg}}$ are taken from the annual mean wind stress climatologies [*Trenberth et al.*, 1989]; normal components of velocity $v_n^{\mathrm{fg}}(\partial\Omega)$ at the open boundaries are computed by dynamical method and corrected within the surface and bottom Ekman boundary layers to take into account wind stresses and the no-slip boundary condition. A constant normal velocity field is added to $v_n^{\mathrm{fg}}(\partial\Omega)$ to bring the first-guess total transport through the model domain to zero.

[19] The cost function contains four basic groups of terms denoted by roman numbers. The first group represents weighted sums of squared differences between the data (denoted by stars) and their model counterparts. The second group of terms penalizes large deviations of optimal control vector from the first guess estimate and makes the assimilation problem formally well posed. Here V_k denotes the total transport through the kth open boundary and V_k^{fg} is the first-guess estimate of this transport. The three open boundaries are the Bering and Denmark Straits and the Norway-Iceland opening (Figure 1). The third group of terms penalizes errors $\varepsilon_{\theta,S}$ in the tracer conservation equations. The first two terms penalize the residuals in each node with the weights W_ε depending on horizontal coordinates and depth. The next two terms in group III introduce our expectation that the vertically integrated residuals $\bar{\varepsilon}_{\theta,S}$ within each water column should be essentially smaller than the typical magnitude of $\varepsilon_{\theta,S}$. This means that potential temperature and salinity are redistributed within a water column rather than created by the sub-grid processes. Group IV represents the so-called regularization terms that penalize horizontal grid-scale variability of horizontal velocity in the vicinity of open boundary and the amplitude $\|\mathbf{u}_b\|_k$ of the stabilization components of the velocity field. These terms are primarily introduced to avoid formation of artificial boundary layers at the open boundaries, and their weights are much smaller in the interior of the model domain.

[20] We interpret $\mathcal{J}$ as the argument of a prior Gaussian probability density, so the weights W are the inverse covariance matrices for the model or model-data errors. They are assumed to be diagonal; that is, errors at different locations are statistically independent.

[21] Diagonal elements of $W_{\theta,S}$ are taken to be inversely proportional to the squared error variances $\sigma^2_{\theta,S}(x, y, z)$ of

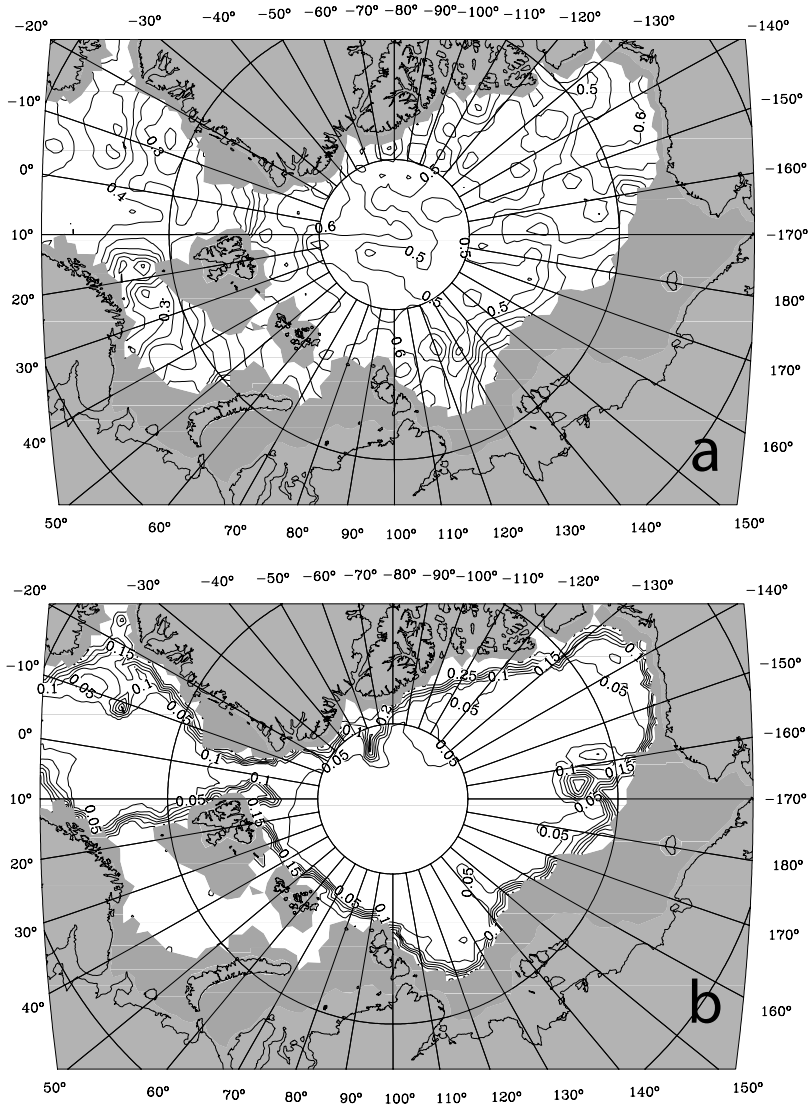

Figure 2. Horizontal distributions of the salinity errors (a) σ_S^{obs} and (b) σ_S^{mod} at 200 m. Contours are in parts per thousand.

EWG data. Assuming spatial inhomogeneity of $\sigma_{\theta,S}$ (Figure 2) allows us to take into account relative undersampling of polar regions and inhomogeneities in variability of θ/S data in the deep layers of the ocean.

[22] Our estimate of $\sigma_{\theta,S}$ has several components. First of all, $\sigma_{\theta,S}$ includes the error of optimal interpolation σ^{OI} of the EWG data, which is well documented in the atlas (Figure 2a; Figure 3, line 1). We also assume that the model-data misfit may contain a component σ^{mod} caused by processes unexplained by our large-scale dynamical model (such as the effects of the eddy dynamics on the large-scale flow, river run-off, interaction with steep topography, etc.). Contribution of these processes to the model-data misfit fields should be treated as noise. We assume spatial inhomogeneity of σ^{mod} and ascribe higher values of this error component on steep topographic features and continental shelves (Figure 2b; Figure 3, line 2). The third source of errors is the temporal variability of the real ocean on intraseasonal to intradecadal timescales. This error component σ^t (Figure 3, line 3) was estimated from the data as a fraction of the RMS difference between winter and summer climatologies at a data point. Near the surface, σ^t exceeds both the optimal interpolation and model errors, while below 75 m, σ^t becomes much smaller than σ^{OI} and σ^{mod} and turns out to be even smaller than uncertainties in the definition of the optimal interpolation and modeling errors. Nevertheless, we did take it into account by specifying the total error of the temperature and salinity fields (Figure 3, line 4) as $\sigma_{\theta,S}(\mathbf{r}, z) = [(\sigma_{\theta,S}^{OI})^2 + (\sigma_{\theta,S}^{mod})^2 + (\sigma_{\theta,S}^{t})^2]^{1/2}$.

[23] Detailed analysis of $\sigma^t(x, y, z)$ has shown, in particular, that seasonal variations of temperature and salinity in the upper 75 m are too high for data assimilation with the steady state tracer conservation constraints. We eliminated these constraints in the upper layer by putting $W_\varepsilon(z < 75\ \text{m}) = 0$. An alternative possibility was to introduce seasonal trends into the tracer conservation equations at these depths. In that case, we would have needed an advanced model of the upper mixed layer and, what is more important, reasonable estimates of the surface heat and FW fluxes. Preliminary analysis of the existing surface heat/FW flux data in AO have shown, however, that their formal errors often exceed the corresponding means. Therefore we

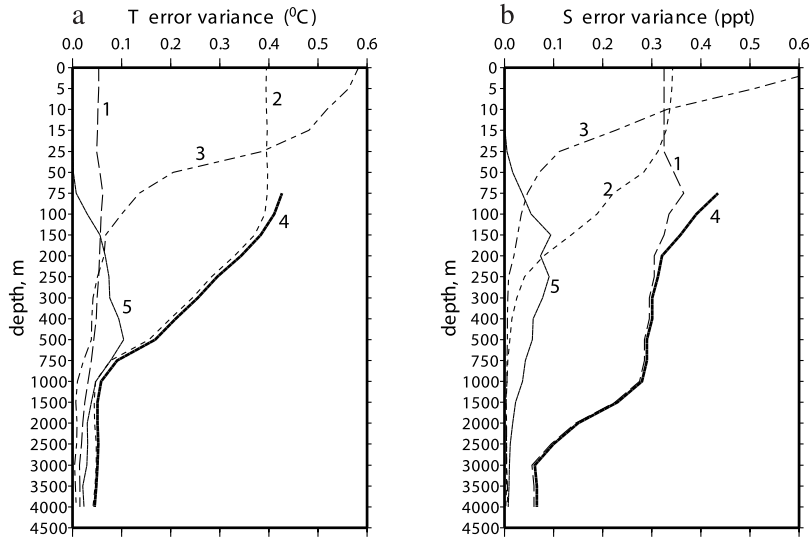

Figure 3. Vertical distributions of the prior error variances σ^{OI} (lines 1), σ^{mod} (lines 2) and σ^{t} (lines 3) in the potential (a) temperature and (b) salinity fields. The net error variances are shown by thick solid lines (lines 4). Lines 5 show model-data misfits after assimilation.

elected to exclude the upper mixed layer from consideration since this reduces the overall uncertainty of the prior probability distribution and provides smaller posterior errors. Nevertheless, inverse solutions in the upper 75 m were kept constrained by the data, momentum balance, hydrostatics, and continuity.

[24] We assessed a formal error of the *Trenberth et al.* [1989] wind stress data as one third of its standard deviation, that is, $\sigma_\tau^{obs} = 0.5$ cm^2 s^{-2}. The surface momentum flux error associated with the absence of an ice model σ_τ^{mod} was assumed to be statistically independent of σ_τ^{obs} and equal to 0.7 cm^2 s^{-2}, so that the total prior error variance of the momentum flux at the ocean surface is 0.85 cm^2 s^{-2}. Therefore the first guess wind stresses that have a typical magnitude of 0.6 cm^2 s^{-2} were used as a relatively weak constraint.

[25] The weights W_ε were taken to be inversely proportional to $(\sigma_{\theta,S})^2$ divided by the square of the "expected residual timescale" T. The latter was estimated as 6 months for the 3D tracer residuals (penalized by $W_\varepsilon^{\theta,S}$) and $\overline{T}$ = 5 years for their vertical means, i.e., $\overline{W}_\varepsilon^{\theta,S} = (\overline{T}/\sigma_{\theta,S})^2$.

[26] Finally, the error variances for the first-guess total transport estimates through the three open ports of the domain were derived by comparing the first-guess values V_k^{fg} with the transport estimates found in oceanographic literature. The corresponding RMS variances were taken to be 0.4 Sv for the Bering Strait, 1.2 Sv for the Denmark Strait, and 1.0 Sv for the inflow region between Iceland and Norway. Small straits in the Canadian Archipelago were kept closed.

[27] Overall, the discretized form of equations (1)–(3) contains $5N^e + 2N - N_\Gamma = 661{,}885$ independent relationships constraining the state vector Y and the error fields $\varepsilon_{\theta,S}$. The cost function additionally specifies $M = 3N + 3N^e + 2N_\Gamma^e + 2N_\Gamma + 3 = 452{,}277$ "weak" constraints (understood in the least squares sense). The ratio of the number of unknowns $5N^e + 4N = 712{,}563$ to the total number of constraints is 0.64, and the inversion problem can formally be considered as overdetermined. We minimized the cost function using the iterative quasi-Newtonian algorithm of *Gilbert and Lemarechal* [1989]. Cost function gradient was computed using the adjoint of the tangent linear model.

[28] On the total, we performed more than a hundred optimization runs aimed at tuning of the cost function weights and diffusivity coefficients. These experiments have shown reasonable robustness of the inverse solutions within the ranges of variation 10^{-3} – 10^{-4} and 100–1000 m^2/s for the vertical and horizontal diffusion, respectively. We attribute this property to the fact that the problem is highly constrained by the hydrographic data, whereas the Ekman pumping rates that affect the global circulation pattern, do not depend upon the values of K and K^v. Diffusion coefficients in the ocean interior were tuned to minimize the misfit with hydrographic data.

3. Mean Circulation and Its Seasonal Variability

[29] To diagnose the mean flow field of the Arctic Ocean, we assimilated the climatological fields of potential temperature and salinity from the EWG [1998] atlas averaged over 45 years (1948–1993). The resulting winter and summer circulations provide reference patterns for the analysis of interdecadal variability and give an insight into the general structure of the currents and transports for the winter and summer seasons.

[30] The stream function of total transport ψ was computed as a weak (FE) solution of the Poisson equation $\Delta\psi = \omega$, where ω is the curl of the depth-integrated velocity U. The corresponding RMS error σ_ψ was estimated by convolving the inverse of the diagonal approximation of the error covariance matrix $C = \langle U^\dagger U \rangle^{-1}$ with the FE representation of the gradient operator: $\sigma_\psi^2 = (\nabla^\dagger C \nabla)^{-1}$. The typical values of σ_ψ ranged within 0.1–0.2 Sv.

[31] Stream functions of total transport for the mean summer and winter circulations are shown in Figures 4a and 4b. In the following, we define total transports as

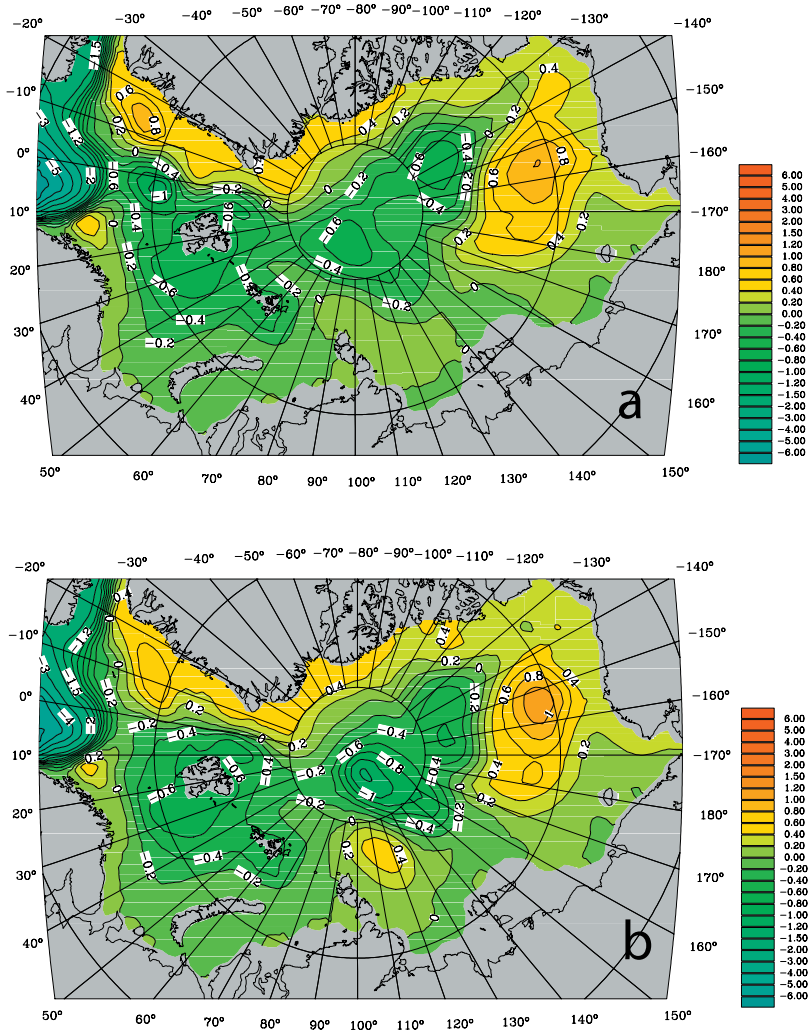

Figure 4. Optimized total transport stream function for the (a) winter and (b) summer EWGM climatologies. Contour units are in Sverdrups.

differences in ψ between the centers and the largest closed contours of the corresponding gyres. The major qualitative feature seen in the patterns is intensification of the transports in the Pacific sector (Figures 1 and 4) of AO in summer. For instance, anticyclonic circulation in the Beaufort Gyre (BG) (155°W, 77°N) spins up from 0.6 ± 0.2 to 0.8 ± 0.3 Sv and shrinks in horizontal size (Figure 4). In winter, BG occupies approximately a 30% larger area than in summer.

[32] Intensification of the total transport in Beaufort Gyre in summer seems to be in contradiction with a well-established notion of BG relaxation in July–October [e.g., *Proshutinsky and Johnson*, 1997; *Proshutinsky et al.*, 2002b]. This relaxation is believed to be caused by weakening of the Ekman convergence that is driven by winds associated with high atmospheric pressure over the Canadian Basin in winter. Results of our computations do agree with that concept and show a considerable reduction of the near-surface circulation in BG that can be diagnosed though relaxation of the associated SSH anomaly (Figure 5). In contrast to SSH, ψ is affected, however, by a number of factors that include the basin-scale structure of the density, SSH, and bottom topography fields. For a simplified case of the geostrophic flow in a flat-bottomed infinite basin, the anomaly of total transport stream function $\delta\psi$ can be expressed in terms of the SSH and depth-integrated baroclinic pressure anomalies $\delta\zeta$ and δp_ρ as follows:

$$\delta\psi = \frac{gH\rho_0\delta\zeta + \delta p_\rho}{f\rho_0} = \frac{gH}{f}\left[\delta\zeta + \int_0^H \frac{\delta\rho(z)}{\rho_0}\left(1 - \frac{z}{H}\right)dz\right]$$

If we assume that δ stands for the difference between the winter and summer values of ψ, ζ, and ρ, then the diagnosed amplification of BG transport $\delta\psi < 0$ in summer can exist when the depth-integrated baroclinic pressure anomaly is negative and $|\delta p_\rho| > g\rho_0 H\delta\zeta$. We found that the optimized density field satisfies this criterion. When averaged over the core of BG (Figure 5), the EWGM density data also produce the depth-averaged pressure anomaly of −180 Pa (Figure 6), which tends to compensate the area-mean seasonal drop in SSH. Although the summer intensification of the total transport in BG is diagnosed at the level close to the formal error bars ($\delta\psi$ = 0.21 ± 0.24 Sv), we do assume

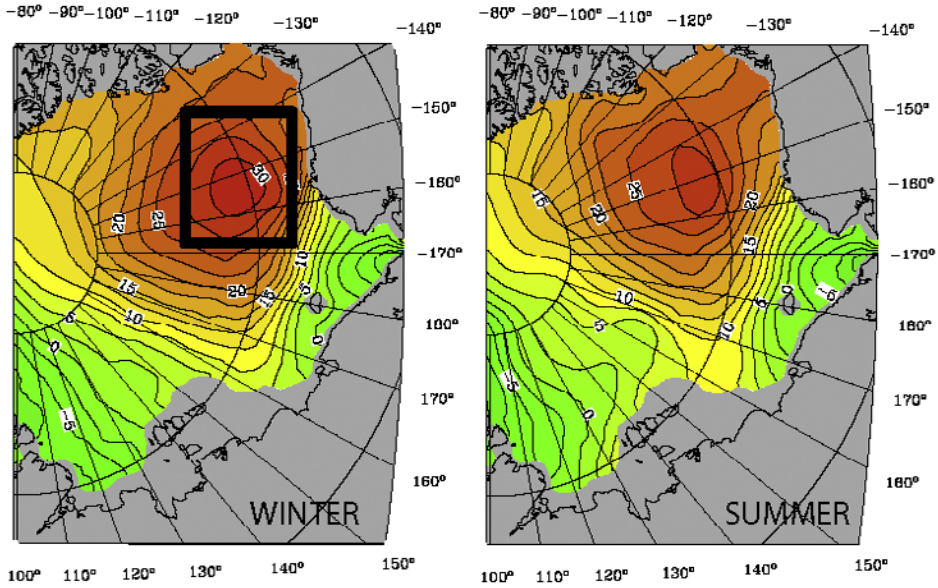

Figure 5. Optimized SSH for the winter and summer EWGM climatologies. Contour units are in centimeters.

that this is a realistic feature of circulation, supported by indirect observational evidence presented in Figure 6.

[33] In winter, on the contrary, a certain amplification of the transports occur in the Atlantic sector of AO (west of 80°E and east of 70°W in Figure 4). This intensification manifests itself by a 10% increase of the transport of the Norwegian Current inflowing the domain at 10°E, by emergence of an intensive cyclonic circulation in the northern Greenland Sea centered at 3°E, 75°N, and by amplification of the anticyclonic gyre off the eastern Greenland coast.

[34] All of the diagnosed changes can be attributed to seasonal variation of both thermohaline and wind forcing. As an example of importance of the wind forcing, *Proshutinsky and Johnson* [1997] and *Zhang et al.* [1999] observed high correlations between surface currents in the eastern part of AO and atmospheric pressure, which tends to have a maximum over BG in winter and a minimum over the polar (Amundsen and Makarov) basins in summer. At the same time, an important summertime thermohaline agent is the 0.2- to 0.25-Sv river discharge, which substantially elevates sea surface at the continental margins (especially in the Siberian sector) and enforces cyclonic circulation in the central Arctic. In winter, the major thermohaline forcing takes place in the Greenland Sea with the onset of deep convection. Our computations trace the signature of deep convection in the form of a localized cyclonic circulation collocated with the positive density anomaly seen in Figure 7 near the intersection of 75°N with the Greenwich meridian. This is a typical winter feature explained by vorticity generation around the convective chimneys [*Marshall and Schott*, 1999]. Moreover, comparison of the winter and summer total transport patterns (Figure 4) gives an indication of the dynamical importance of the vorticity induced by convection: A cyclonic feature centered at 2°E, 76°N in Figure 4a enforces penetration of the ψ contours around Svalbard and farther into the Arctic Basin. In summer (Figure 4b), this cyclone (presumably forced by deep convection) is totally absent, and the stream function contours indicate much weaker exchange between the AO and Atlantic.

[35] Table 1 gives an inventory of the heat and freshwater (FW) transports through the open boundaries of the model domain. Heat transports were computed relative to

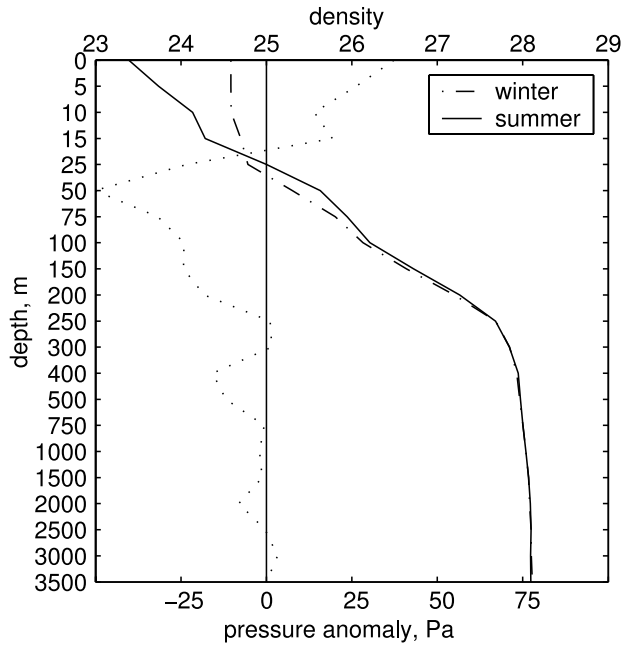

Figure 6. Horizontally averaged density profiles in the Beaufort Gyre for summer (solid line) and winter (dash-dotted line) EWGM climatologies. The averaging area is shown by a bold rectangle in Figure 5. Dotted line shows the mean vertical profile of the baroclinic pressure anomaly $g\delta\rho(z)(1 - z/H)\Delta z$.

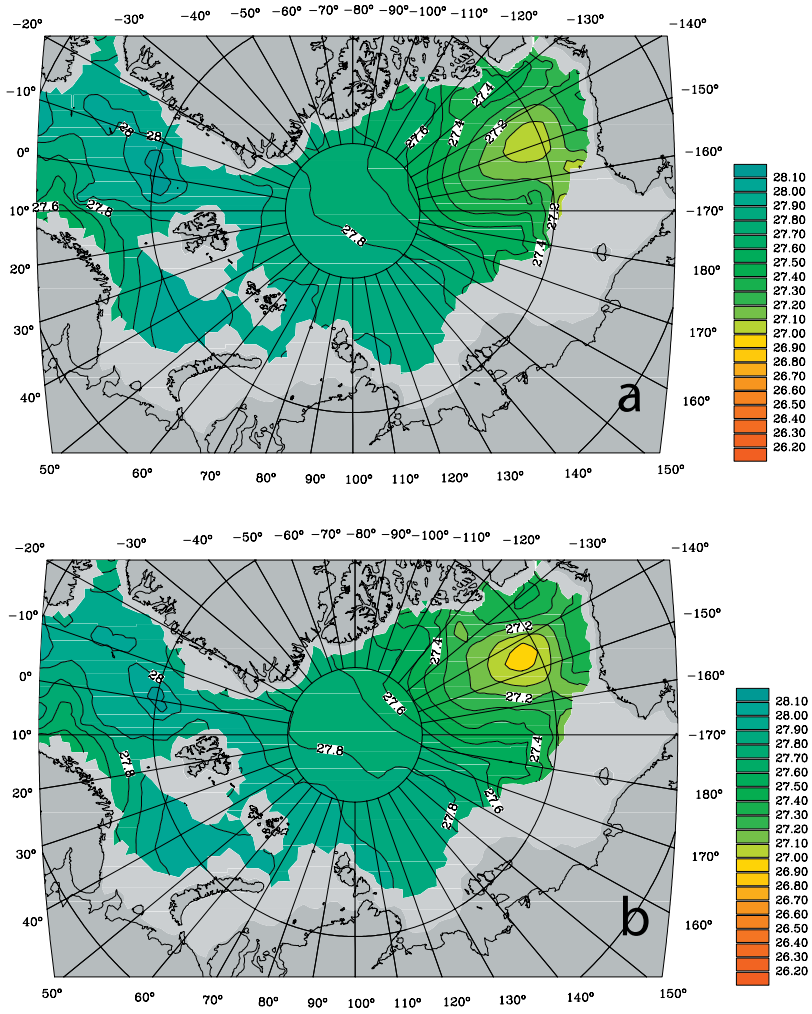

Figure 7. Optimized density fields at 200 m for the (a) winter and (b) summer EWGM climatologies. Contour interval is 0.1 kg/m^3.

−0.295°C, which is the annual mean temperature of the optimal state. Numbers for individual ports may vary by 4–8 × 10^{12}W with the reference temperature variation of 1°C. The total heat and FW fluxes in the last column of Table 1 are, however, invariant due to mass conservation. Dividing the mean heat transport in the last column by the area 1.1 × 10^{13} m^2 of the model domain, one can estimate the annual mean cooling rate of the Arctic Ocean as 16.5 W/m^2. To correctly assess seasonal changes in the cooling rate, it is necessary to take into account the negative heat storage associated with ice formation in winter and its subsequent export in summer. Assuming the total annual mean ice export is 3700 ± 800 km^3/yr [*Aagaard and Carmack*, 1989], we arrive at 20 ± 4 W/m^2 for the average amount of heat lost from the sea surface in the Arctic Basin. This number is consistent with typical estimates of the high-latitude annual mean ocean-atmosphere heat flux [e.g., *Sturm et al.*, 2001].

[36] FW transports were computed relative to the average salinity $\bar{S}$ = 34.758 ppt of the optimal state (the number given by the *EWG* [1998] atlas is 34.760). Sensitivity of the salt transports in the three open ports of the model domain is 30–50 km^3/yr per 0.01 ppt of $\bar{S}$ variation. Statistically significant seasonal changes in the FW balance indicate a 230 ± 140 km^3/yr increase of FW supply (reduction of salt import) through the Norway-Iceland port, which is accompanied by a 530 ± 220 km^3/yr decrease in salt export (FW import) through the Denmark Strait, and by the 270 ± 140 km^3/yr increase of the FW import through the Bering Strait in summer. The net advective FW budget does not exhibit such a strong seasonal variation, because changes in individual transports tend to compensate each other. Nevertheless, there is a tendency for a somewhat smaller FW import in summer, which is possibly associated with an overall reduction of AO salinity due to ice melting and river discharge.

[37] In summary, seasonal variability of the large-scale circulation of the AO is characterized in summer by (1) an increasing cyclonic circulation in the Central Basin and intensification of the BG; (2) development of the anticyclonic gyre in the northern Laptev Sea; (3) reduction of the net ventilation rate in the Atlantic sector, partly associated with the contraction of the convective gyres in the Greenland Sea; and (4) increase of the net advective FW export. These changes, driven by both wind and thermohaline

Table 1. Transports of Heat and Freshwater (FW) Through the Open Boundaries of the Model Domain for the Mean Winter and Summer Climatologies[a]

	Norway/Iceland	Denmark Strait	Bering Strait	Total
		Heat flux, 10^{13}W		
Winter	18.9 ± 0.7	−1.5 ± 0.8	−0.2 ± 1.0	17.2 ± 0.8
Summer	20.8 ± 0.7	−2.3 ± 0.7	0.7 ± 0.9	19.2 ± 0.8
		FW flux, $10^{2}km^{3}/yr$		
Winter	−7.3 ± 1.5	5.6 ± 1.9	7.8 ± 1.3	6.1 ± 1.6
Summer	−5.0 ± 1.4	0.3 ± 2.4	10.5 ± 1.5	5.8 ± 1.8

[a]Positive values denote inflow into AO.

factors, are the signatures of seasonal variability in the atmosphere and surrounding oceans.

4. Decadal Variability

[38] Inversions of the EWG50-80 hydrographies were performed separately for summer and winter seasons. Interdecadal variability was then obtained by averaging seasonal characteristics for each decade.

[39] Winter anomalies of the stream function of total transport are exposed in Figure 8. The major trends in circulation are identified as follows. First, there is an evident intensification of the anticyclonic structures in the Pacific sector manifested by the expansion of positive stream function anomalies in the 1970s and 1980s. That expansion was accompanied by displacement of BG 10° to the east (Figure 9). At the same time, a statistically significant decrease of cyclonic activity in the north Greenland Sea is diagnosed. In the 1970s, the decrease was confined to a small area around the intersection of the Greenwich meridian with 75°N (Figure 8c). A decade later the positive stream function anomaly expanded south and almost doubled in size, invoking a qualitative change of the total transport pattern in the Atlantic sector. In the 1950s, there is a large recirculation around Svalbard and Franz-Josef Land visible at −0.2 and −0.4 Sv contours. Three decades later this connection with the Atlantic does not exist anymore (Figure 9b). We attribute this change to reduction in size of the cyclonic gyre maintained by the deep convection in the northern Greenland Sea. A concentrated anticyclonic stream function anomaly at 0° 76°N emerged due to shrinking of the "convective" density maximum

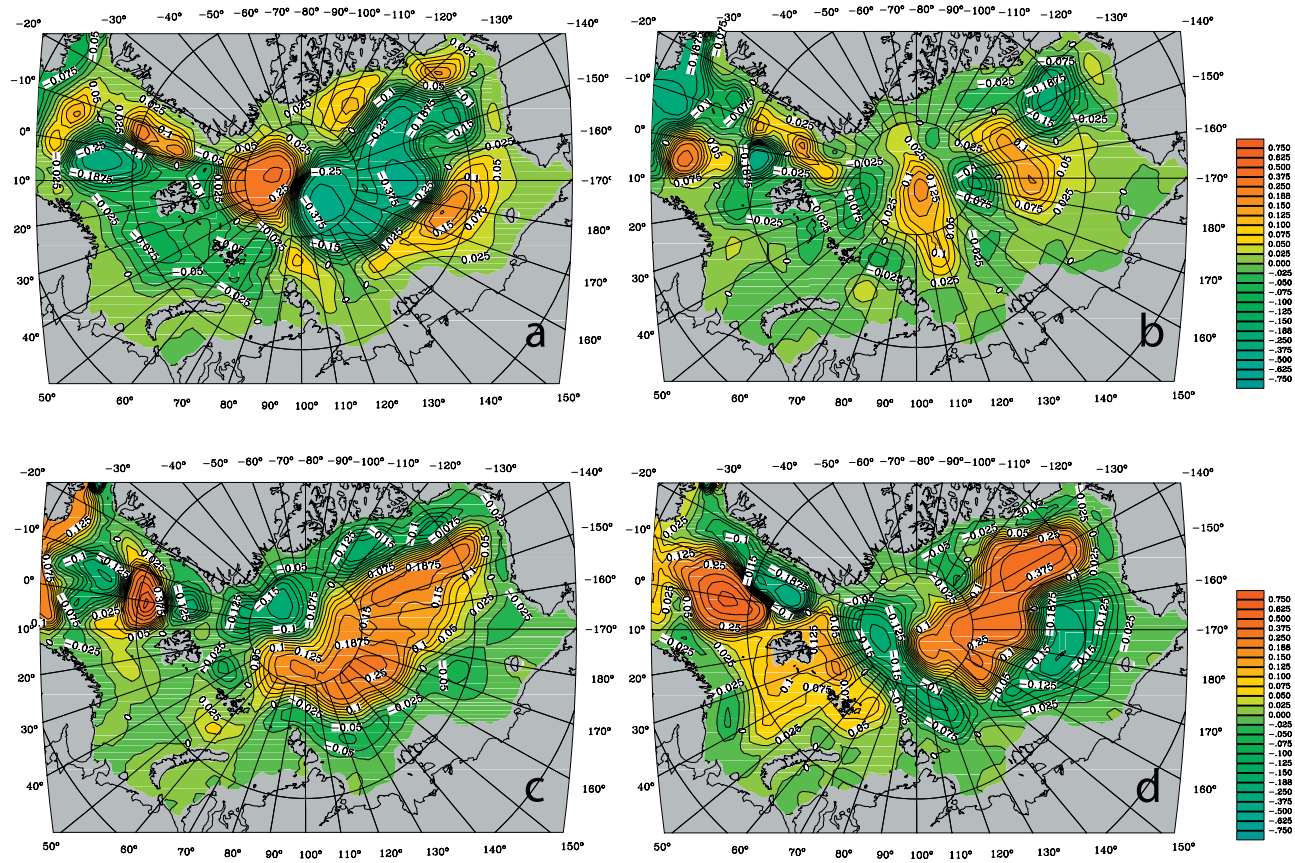

Figure 8. Anomalies of the optimized stream function of total transport for the winter (a) EWG50, (b) EWG60, (c) EWG70, and (d) EWG80 climatologies. Contour units are in Sverdrups.

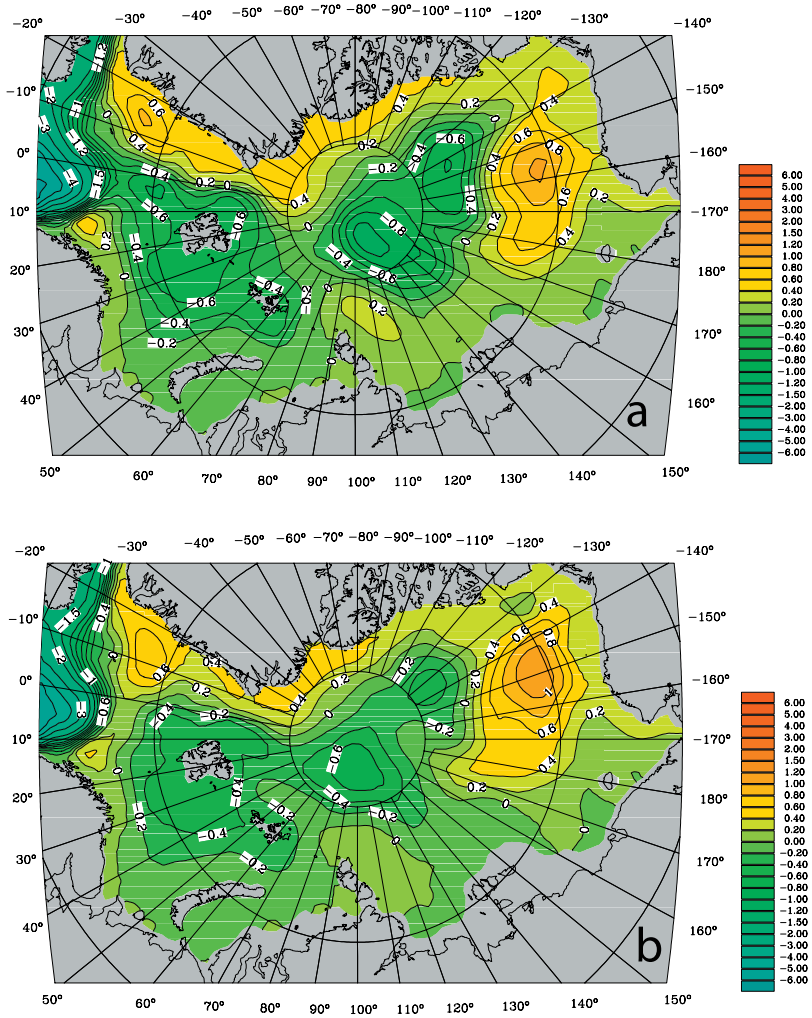

Figure 9. Stream function of total transport for (a) EWG50 and (b) EWG80 climatologies. Contour units are in Sverdrups.

(Figures 10a and 10b). In the 1980s (Figure 8d), the anomaly was possibly dispersed by mesoscale eddies and further enforced by weakening convection. In these two aspects (amplification of BG and reduction of cyclonic activity in deep convection region), the observed interdecadal changes in the barotropic circulation are similar to those diagnosed at the transition from winter to summer; that is, the trend may indicate a certain shift in the direction of a warmer climate over AO.

[40] Optimized transports at the open boundaries give further evidence of the shift that manifests itself by a certain decrease of the advective import of heat, FW, and reduction of the net ventilation rate of the Arctic Ocean, defined as the total volume transport into the model domain. Figure 11 shows decadal values of these transports together with the estimates of their long-term trends. Since the Bering Strait contribution is small, the ventilation rate variability is defined by variations in the exchange of waters with the Atlantic Ocean. Our computations diagnose a maximum of 11.3 ± 0.9 Sv in the 1960s, and since then the ventilation rate was gradually decreasing to 9.7 ± 0.6 Sv. The variations of the Bering Strait transport were about 0.1–0.2 Sv, and did not contribute significantly to the overall trend of $-.024 \pm .038$ Sv/yr. This value turns out to be statistically indistinguishable from zero due to the small value (10.1 ± 0.7 Sv) diagnosed in the 1950s. Nevertheless, the 10% reduction of ventilation observed since the 1960s is statistically significant, and we believe it is directly connected to the weakening of cyclonic gyre in the northern Greenland Sea, which is partly forced by the deep convection.

[41] Heat fluxes demonstrate a statistically significant decreasing trend in the advective import of heat at a rate $0.52 \pm 0.44 \times 10^{12}$ W/yr. Under the assumption of thermal equilibrium, that number converts to reduction of the annual mean surface cooling rate by 1.3 ± 1.1 W/m^2 over the last decades, and indicates certain warming of the AO surface waters. It is noticeable, however, that although the optimized amount of heat imported with Atlantic waters increased by $0.8 \pm 1.1 \times 10^{13}$ W, the net effect remains negative due to a $2.2 \pm 1.9 \times 10^{13}$ W increase of the heat export by the deep outflow of Arctic waters.

[42] FW fluxes demonstrate a dramatic drop in the outflow of salt or, equivalently, a 610 ± 220 km^3 increase of the FW export between the 1950s and 1960s, which is related to freshening of the AO outflow associated with the "great salinity anomaly" [*Dickson et al.*, 1988]. FW export

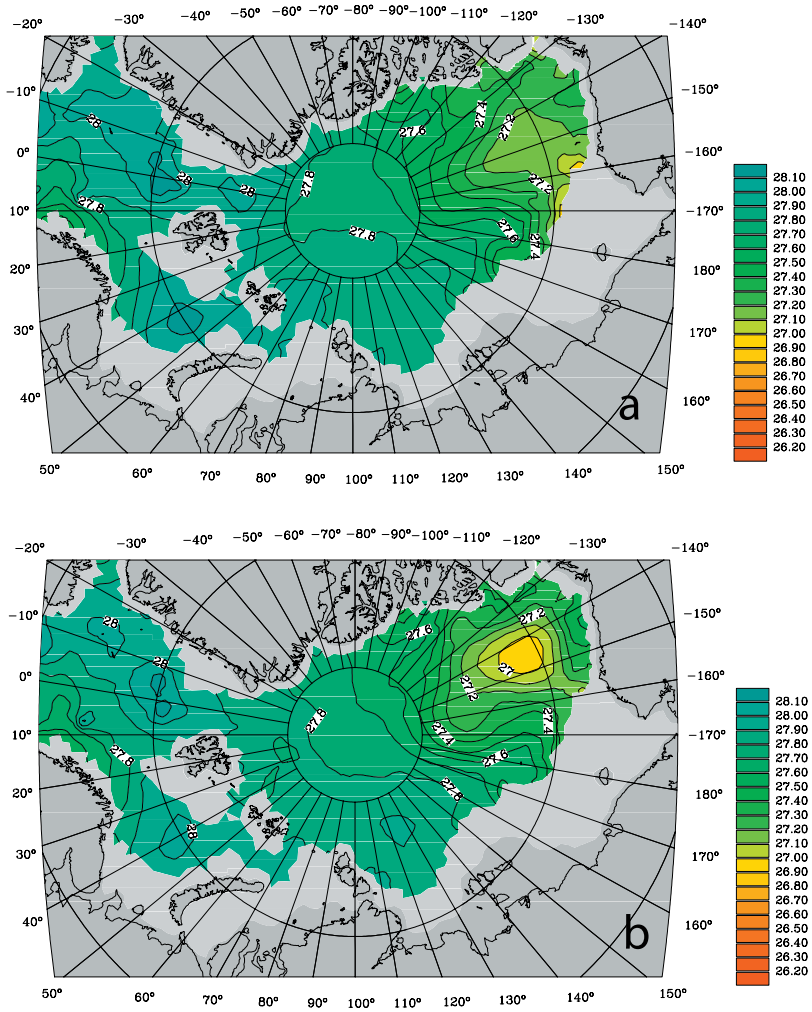

Figure 10. Interdecadal variation of the optimized density field at 200 m for the winter (a) EWG50 and (b) EWG80 climatologies. Contour interval is 0.1 kg/m^3.

continued to grow in subsequent decades, although at a lower rate (Figure 11). According to our computations, the observed trend in the net advective FW export is governed by two factors: (1) an increase of the amount of salt imported with Atlantic waters between the 1950s and 1980s, and (2) a 210 ± 170 km^3 growth of the FW export through the Denmark Strait (Figure 12). FW import through the Bering Strait did not show any statistically significant trend because a 230 ± 180 km^3 drop in the 1960s was compensated by the 200 ± 190 km^3 increase in the 1970s and 1980s.

[43] In the analysis, we do not consider several important constituents of the FW budget, namely, the river runoff (3300 km^3/yr), P-E (900km^3/yr) and ice export through the Fram Strait and Canadian Archipelago (3700 km^3/yr; the estimates are taken from [*Aagaard and Carmack*, 1989]). Both optimized and EWG salinity fields show that imbalance between these constituents and the advective transports in Figure 11 is likely to have been growing in favor of freshening of the AO. This indicates existence of a FW source in the basin that overpowers the advective drainage by geostrophic currents. Recovering the nature of this source is far beyond the scope of the present study, although we can speculate that it is powered by warming of the Arctic climate.

[44] Following the technique of *Aagaard and Carmack* [1989], we assessed FW storage in the Pacific and Atlantic sectors of the Arctic Ocean (Table 2). In contrast with the Pacific sector, which was gaining FW at a nearly constant rate of 35 km^3/yr, the Atlantic sector was subject to a rapid growth of FW storage in the last 2 decades at the rates of 130–150 km^3/yr. From the qualitative point of view, that difference is consistent with almost 2 times faster thinning of the ice cover over the Atlantic sector [*Rothrock et al.*, 1999]. A recent modeling/observational study by *Holloway and Sou* [2002] indicates, however, that a significant portion of ice thinning documented by *Rothrock et al.* [1999], may be caused by advective redistribution of ice mass in the Arctic Basin. Quantitatively, the estimate of *Holloway and Sou* [2002] is in better correspondence with the FW content trends obtained in the present study. These trends can be explained by thinning of the permanent ice cover at the rates of 1 and 2 cm/yr for the Pacific and Atlantic sectors, respectively. We should also note that the revealed trends in the FW content are also present in EWG data, and the observed freshening of the Atlantic sector is in agreement

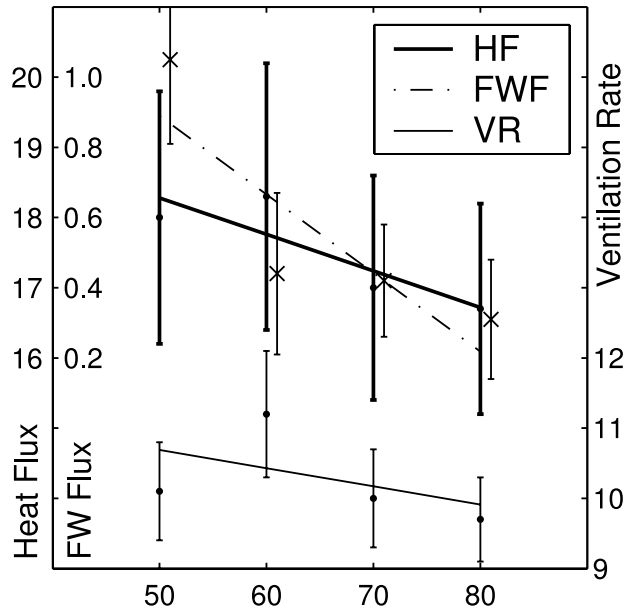

Figure 11. Advective transports of heat, freshwater (FW), and the ventilation rate of the model domain for the annual mean EWG50-80 climatologies. Positive values denote inflow into AO. The units are 10^{12} W, 1000 km^3/yr, and Sverdrups for the heat, FW, and ventilation rate, respectively.

with the concept of gradual transition of AO circulation to the cyclonic regime that was observed in the 1980s and 1990s [*Proshutinsky and Johnson*, 1997; *Proshutinsky et al.*, 2002b].

[45] Indications of desalinization trends are seen in optimal solutions and reach even the abyssal layers. Figure 13 shows salinity anomalies at 2000 m after optimization. The Pacific sector is characterized by the average salinity loss at a rate of $3 \pm 2 \times 10^{-5}$ ppt/yr. Although this value (0.0015 ppt over 50 years) is within the formal error bars for salinity measurements and can be considered as zero for all practical purposes, we do assume that it may indicate the overall direction of evolution of the deep water masses over the last 5 decades.

[46] Inverse analysis of the EWG climatologies reveals interdecadal changes in the AO state that qualitatively agree with those typical for transition from winter to summer season, i.e., with the concept of gradual warming of the Arctic climate. The trends show reduction of the AO ventilation rate that is accompanied by the enhanced

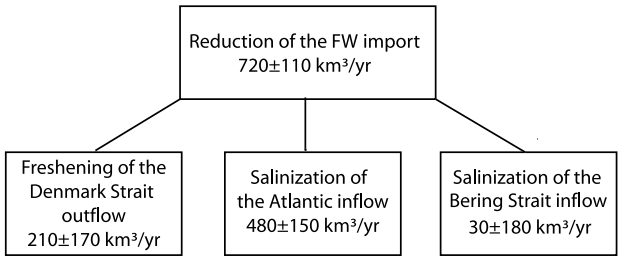

Figure 12. Constituents of the interdecadal trend in the net advective FW budget for the Arctic Ocean.

Table 2. Decadal Variability of the Net Freshwater Storage (10^4 km^3, Relative to 34.93 ppt) in the Atlantic and Pacific Sectors (see Figure 1) of the Arctic Ocean

Data Set	Atlantic Sector	Pacific Sector	Total
EWG50	1.45 ± 0.08	5.72 ± 0.06	7.17 ± 0.07
EWG60	1.44 ± 0.06	5.75 ± 0.05	7.20 ± 0.05
EWG70	1.52 ± 0.07	5.78 ± 0.05	7.31 ± 0.06
EWG80	1.69 ± 0.07	5.82 ± 0.05	7.51 ± 0.06

advective export of FW and heat and desalinization of the Arctic Basin.

5. Summary

[47] In this study, we have used an inverse finite-element model to analyze the mean seasonal and interdecadal variability of the Arctic Ocean. In contrast to recent pure modeling studies [e.g., *Zhang and Hunke*, 2001; *Zhang et al.*, 1998], we employed an approach that puts more emphasis on data and have found model solutions which are statistically consistent with EWG climatologies. Given moderate skill of the existing ice models and poor accuracy of surface forcing climatologies, we refrained from attempts to simulate upper layer thermodynamics and focused on the retrieval of the large-scale nearly geostrophic flow, assuming that EWG hydrography provides much better approximation to reality above the 50 m depth than any upper layer/ice model forced by uncertain atmospheric fluxes. Following this ideology, we successfully reconstructed the large-scale barotropic flow in the Arctic Ocean, which is consistent with continuity, momentum, and θ/S conservation constraints. As a byproduct of optimization, we obtained estimates of the open boundary transports, which are "necessary" to maintain the observed temperature and salinity distributions. The estimates are supplied with error bars deduced from the ensemble of assimilation runs. In the above aspects, our analysis supplements direct modeling studies that derive AO state from surface and open lateral boundary fluxes under the assumption of their infinite accuracy.

[48] Major results of the study are in line with the well-known concept of "Arctic warming," which manifests itself by the increasing advection of heat from the Atlantic [*Dickson et al.*, 2000], freshening of the upper ocean, thinning and shrinking of the ice cover [*Rothrock et al.*, 1999; *Holloway and Sou*, 2002], and degrading convection in the Greenland Sea [*Marshall and Schott*, 1999]. The exact mechanism that causes Arctic warming is still unknown. However, it may be related to large-scale atmospheric phenomena occurring on interannual scales like the North Atlantic Oscillation [*Dickson et al.*, 2000; *Polyakov and Johnson*, 2000] or Arctic Oscillation [*Thompson and Wallace*, 1998; *Ikeda et al.*, 2001].

[49] Our present goal was to retrieve changes in the AO large-scale circulation from the available data and estimate open boundary forcing that may play an important role in AO variability. The analysis, although diagnostic in nature, reveals some important dynamical features accompanying the warming trend. We diagnose a 10–15% reduction of the surface circulation in BG that is accompanied by amplification of its total transport. Our analysis, and EWG clima-

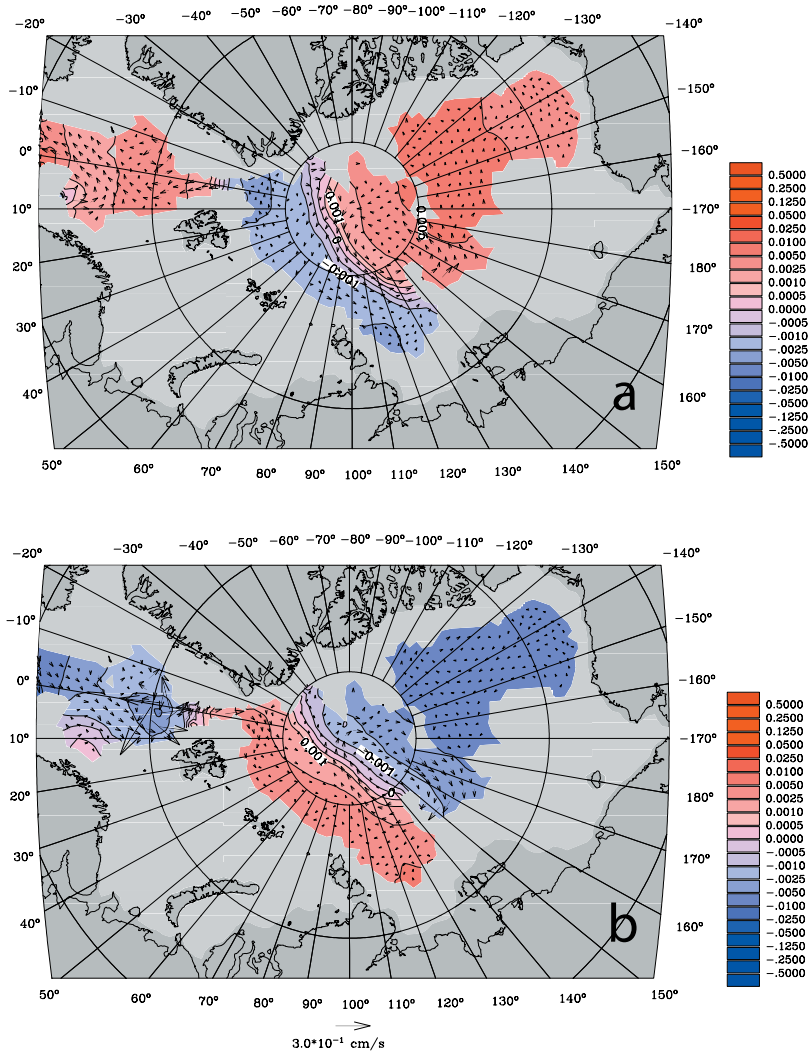

Figure 13. Optimized salinity and velocity field anomalies at 2000 m derived from the winter (a) EWG50 and (b) EWG80 climatologies.

tologies as well, reveal an overall increase of the FW content in the Arctic, with the major contribution given by the Atlantic sector. Amplification of the BG total transport may be connected to the gradual increase of density throughout the water column in the Canadian Basin. The corresponding trend in baroclinic pressure anomaly appears to be larger than the one caused by decreasing SSH anomaly, and results in 0.21 ± 0.24 Sv increase of the BG total transport.

[50] Our computations also show that AO ventilation rate has decreased from 11.4 ± 0.8 Sv to 9.7 ± 0.6 Sv in the last 3 decades. We speculate that this reduction may partly be caused by fading convection that drives the cyclonic gyre in the northern Greenland Sea. Spinning the gyre down may reduce the supply of deep and relatively fresh Arctic water through the Fram Strait, resulting in further abyssal salinization and increasing stratification in the convective regions of the north Greenland Sea.

[51] It is noteworthy that in recent modeling studies, *Polyakov et al.* [1999] and *Zhang and Hunke* [2001] observed weakening of the AO anticyclonic circulation in the upper ocean between the late 1980s and 1990s. In their models, the process is caused by switching of the wind forcing form anticyclonic to cyclonic regime in the late 1980s. The importance of these alterations in atmospheric circulation over AO on interannual timescale was probably first noted by *Proshutinsky and Johnson* [1997]. Integrating a 0.5° resolution barotropic model of the AO, they revealed six alterations between the cyclonic and anticyclonic regimes of the upper ocean currents, which seemed to be in good agreement with drifting buoy trajectories. Although decadal EWG climatologies overlap the transition periods of Proshutinsky and Johnson, the 1950s and 1970s can be roughly classified as anticyclonic, whereas the 1960s and 1980s tend to be cyclonically dominated with a weak overall trend towards "cyclonization" of the upper ocean currents over the 4 decades. Proshutinsky and Johnson used a time-evolving barotropic model without data assimilation, and it is hard to expect high correlation between their SSH anomalies and our diagnostic results. Nevertheless, we did observe a certain increase of the cyclonic vorticity index in the optimized upper layer currents between the 1950s and 1980s. The corresponding "cyclonization" trend appeared to be below the 70% confidence limits, and we could not

draw any definite conclusions on whether it is due to insufficient statistics or whether the overall amplification of cyclonic structures in the upper layer could be a general long-term trend caused by freshening of the AO that is documented in EWG climatologies. Anyway, the revealed trend seems to agree with the concept of "cyclonization" of the surface currents in the past decades put forward by *Proshutinsky and Johnson* [1997].

[52] Advective fluxes at the open boundaries demonstrate statistically significant trends that correspond to the decrease of the AO cooling rate and FW supply (salt export) by 1.3 ± 0.9 W/m^2 and 720 ± 130 km^3/yr, respectively, over the last 4 decades. Our computations show that the Bering Strait plays a minor role in the heat budget, so that the net change in the advective heat flux is defined by two major opposite trends: a 0.8 ± 1.1 W m^{-2} increase of the heat import with the Atlantic water, and a 2.2 ± 1.9 W m^{-2} increase of the heat export with the deep Arctic outflow. The net advective FW flux is determined by the balance between the FW inflow through the Bering Strait, FW outflow through the Denmark Strait, and salt import from the Atlantic. The dominating factors affecting interdecadal trend in the advective FW budget were the 210 ± 170 km^3/yr increase of the FW export through the Denmark Strait, and a rapid increase of the salt import from the Atlantic, which effectively decreased FW import by 480 ± 150 km^3/yr between the 1950s and 1980s. Changes in FW import through the Bering Strait did not show any statistically significant trend.

[53] Despite reduction of advective FW supply, average salinity of the optimized AO states appeared to be 0.008 ± 0.006 ppt less in the 1980s compared to the 1950s. The same trend is observed in EWG data. This phenomenon can be explained if we assume that the surplus of FW released at the surface annually by excessive melting [*Holloway and Sou*, 2002] is accumulated in the Arctic Basin. The diagnosed freshening of the Arctic waters causes an increase of their buoyancy, especially in the upper layers, and may eventually shut down the deep convection in the North Atlantic.

[54] In the present study, we have assessed only advective constituents of the net FW budget in the AO. Other important factors include river runoff, precipitation minus evaporation, ice export, and the Canadian archipelago throughflow. Taking these into account can change the results quantitatively, but, we believe, not qualitatively, since the model states are heavily constrained by hydrography. Further improvement of the model's performance can be achieved by grid refinement to resolve fine topography of the Canadian Archipelago, taking river runoff into the account, and supplying a reliable ice model. These changes will upgrade the set of dynamical and statistical constraints and provide better opportunities for explicit retrieval of the FW and heat budgets in the Arctic Ocean from climatological data.

[55] **Acknowledgments.** This study was supported by the NOAA/CIFAR grant UAF-00-0080, and the Frontier System of Global Change through its funding of the International Pacific Research Center (IPRC). This manuscript is IPRC/SOEST contribution 250/6556.

References

Aagaard, K., and E. C. Carmack (1989), The role of sea ice and other fresh water in the Arctic circulation, *J. Geophys. Res.*, *94*, 14,485–14,498.

Ambaum, M. H. P., B. J. Hoskins, and D. B. Stephenson (2001), Arctic Oscillation or North Atlantic Oscillation?, *J. Clim.*, *14*, 3495–3507.

Dickson, R. R., J. Meincke, S.-A. Malmberg, and A. J. Lee (1988), The "great salinity anomaly" in the northern North Atlantic 1966–1982, *Prog. Oceanogr.*, *20*, 103–151.

Dickson, R. R., T. J. Osborn, J. W. Hurrell, J. Meincke, J. Blindheim, B. Adlandsvik, T. Vinje, G. Alekseev, and W. Maslowski (2000), The Arctic response to the North Atlantic Oscillation, *J. Clim.*, *13*, 2671–2696.

Environmental Working Group (EWG) (1998), *Joint US-Russian Atlas of the Arctic Ocean* [CD-ROM], Natl. Snow and Sea Ice Data Cent., Boulder, Colo.

Gilbert, J. C., and C. Lemarechal (1989), Some numerical experiments with variable-storage quasi-Newton algorithms, *Math. Prog.*, *45*, 407–435.

Grotov, A. S., D. A. Nechaev, G. G. Panteleev, and M. I. Yaremchuk (1998), Large scale circulation in the Bellingshausen and Amundsen Seas as a variational inverse of climatological data, *J. Geophys. Res.*, *103*, 13,011–13,022.

Hollinger, J. P., R. Lo, G. Poe, R. Savage, and J. Pierce (1987), *Special Sensor Microwave/Imager User's Guide*, Nav. Res. Lab., Washington D. C.

Holloway, G., and T. Sou (2002), Has Arctic sea ice rapidly thinned?, *J. Clim.*, *15*, 1691–1701.

Ikeda, M., J. Wang, and J.-P. Zhao (2001), Hypersensitive decadal oscillations in the arctic/subarctic climate, *Geophys. Res. Lett.*, *28*, 1275–1278.

Ishizaki, H. (1994), A simulation of the abyssal circulation in the North Pacific Ocean, *J. Phys. Oceanogr.*, *24*, 1941–1954.

Karcher, M. J., and J. M. Oberhuber (2002), Pathways and modification of the upper and intermediate waters of the Arctic Ocean, *J. Geophys. Res*, *107*(C6), 3049, doi:10.1029/2000JC00053.

Kondratyev, K. Y., A. Buznikov, and O. Pokrovsky (1995), *Global Change and Remote Sensing: The Russian Experience*, John Wiley, Hoboken, N. J.

Marshall, J., and F. Schott (1999), Open-ocean convection: Observations, theory, and models, *Rev. Geophys.*, *37*, 1–64.

Nechaev, D. A., J. Schröter, and M. Yaremchuk (2003), A diagnostic stabilized finite-element ocean circulation model, *Ocean Modell.*, *5*, 37–63.

Polyakov, I. V., and A. Y. Johnson (2000), Arctic decadal and interdecadal variability, *Geophys. Res. Lett.*, *27*, 4097–4100.

Polyakov, I. V., A. Y. Proshutinsky, and M. A. Johnson (1999), Seasonal cycles in two regimes of the Arctic climate, *J. Geophys. Res.*, *104*, 25,761–25,788.

Proshutinsky, A. Y., and M. A. Johnson (1997), Two circulation regimes of the wind-driven Arctic Ocean, *J. Geophys. Res.*, *102*, 12,493–12,514.

Proshutinsky, A., et al. (2001), The Arctic Ocean Model Intercomparison Project (AOMIP), *Eos Trans. AGU*, *82*, 637–644.

Proshutinsky, A., R. Gerdes, S. Hakkinen, D. M. Holland, G. Holloway, W. Maslowski, M. Steele, and J. Wang (2002a), The Arctic Ocean Model Intercomparison Project (AOMIP) report, pp. 70–73, Int. Arct. Res. Cent., Fairbanks, Alaska.

Proshutinsky, A., R. H. Bourke, and F. A. McLaughlin (2002b), The role of Beaufort Gyre in Arctic climate variability: Seasonal to decadal time scales, *Geophys. Res. Lett.*, *29*(23), 2100, doi:10.1029/2002GL015847.

Rigor, I., and A. Heiberg (1997), International Arctic buoy program data report, 1 January 1996–31 December 1996, *APL-UW TM 05-97*, Appl. Phys. Lab., Univ. of Wash., Seattle.

Rigor, I. G., J. M. Wallace, and R. L. Colony (2002), Response of sea ice to Arctic Oscillation, *J. Clim.*, *15*, 2648–2663.

Rothrock, D. A., Y. Yu, and G. A. Maykut (1999), Thinning of the Arctic sea-ice cover, *Geophys. Res. Lett.*, *26*, 3469–3472.

Steele, M., D. Thomas, D. Rothrock, and S. Martin (1996), A simple model study of the Arctic Ocean FW balance, 1979–1985, *J. Geophys. Res*, *101*, 20,833–20,848.

Steele, M., R. Morley, and W. Ermond (2001a), PHC: A global ocean hydrography with a high quality Arctic Ocean, *J. Clim.*, *14*, 2079–2087.

Steele, M., W. Ermold, G. Holloway, S. Häkkinen, D. M. Holland, M. Karcher, F. Kauker, W. Maslowski, N. Steiner, and J. Zhang (2001b), Adrift in the Beaufort Gyre: A model intercomparison, *Geophys. Res. Lett.*, *28*, 2838–2935.

Sturm, M., J. Holmgren, and D. Perovich (2001), Spatial variations in the winter heat flux at SHEBA: Estimates from snow-ice interface temperatures, *Ann. Glaciol.*, *33*, 213–220.

Thompson, D. W. J., and J. M. Wallace (1998), The Arctic Oscillation signature in the wintertime geopotential and temperature fields, *Geophys. Res. Lett.*, *25*, 1297–1300.

Trenberth, K., J. Olson, and W. Large (1989), A global ocean wind stress climatology based on ECMWF analyses, *Tech. Rep. NCAR/TN-338+STR*, Natl. Cent. for Atmos. Res., Boulder, Colo.

Wadhams, P., and N. R. Davis (2000), Further evidence of ice thinning in the Arctic Ocean, *Geophys. Res. Lett.*, *27*, 4097–4100.

Wallace, J. M. (2000), North Atlantic Oscillation/annular mode: Two paradigms-one phenomenon, *Q. J. R. Meteorol. Soc.*, *126*, 791–805.

Wang, J., and M. Ikeda (2000), Arctic Oscillation and Arctic sea ice oscillation, *Geophys. Res. Lett.*, *27*, 1287–1290.

Zhang, J., W. D. Hibler, M. Steele, and D. A. Rothrock (1998), Arctic ice-ocean modeling with and without climate restoring, *J. Phys. Oceanogr.*, *28*, 191–217.

Zhang, Y., and E. C. Hunke (2001), Recent Arctic change simulated with a coupled ice-ocean model, *J. Geophys. Res.*, *106*, 4369–4390.

Zhang, Y., W. Maslowski, and A. J. Semtner (1999), Impact of mesoscale ocean currents on sea ice in high-resolution Arctic ice and ocean simulations, *J. Geophys. Res.*, *104*, 18,409–18,429.

M. Ikeda, Department of Earth and Environmental Sciences, Hokudai University, Sapporo, Japan. (mikeda@ees.hokudai.ac.jp)

D. Nechaev, Department of Marine Science, University of Southern Mississippi, Stennis Space Center, MS 39529, USA. (dnechaev@ssc.usm.edu)

M. Yaremchuk, International Pacific Research Center, Honolulu, HI, USA. (maxy@soest.hawaii.edu)